lectronic Supplementary Material (ESI) for Journal of Materials Chemistry A.

This journal is © The Royal Society of Chemistry 2022

Supporting Information

Electrochemically Deposited Ordered Hierarchical Metal–Organic Framework-Based Dual-Module Sensor for Decoding Organic Vapors

Sijia Qin, Min Chen*, and Limin Wu*

Department of Materials Science, State Key Laboratory of Molecular Engineering of Polymers, Fudan University, Shanghai, 200433, China

*E-mail: chenmin@fudan.edu.cn, lmw@fudan.edu.cn

Materials. All chemical reagents were purchased from commercial sources and were used as supplied without further purification. Terbium nitrate pentahydrate (99.9%), europium nitrate hexahydrate (98%+), thiophene-2,5-dicarboxylic acid (98%+), methanol (GR), and tetrahydrofuran extra pure (99.5%) were purchased from Aladdin. Size standard microspheres (300 nm, 5%) was purchased from the shanghai hugebio technology company. FTO was commercially available and used as received.

Measurements. X-ray diffraction (XRD) measurements were carried out at room temperature on a Bruker D8 advance fitted using Cu Kα (λ=1.5418 Å) radiation. The scan sped and step size of the measurements were 5 degree/min and 0.02, respectively. Fluorescence spectra and lifetimes were recorded on the Edinburgh Instruments FLS 1000. Quantum yields were measured in QCM40. The transient PL spectra were measured on a photoluminescence spectrometer at 77K. The surface morphology of the MOF-based film was examined by a FESEM Zeiss Ultra 55. Energy dispersive X-ray analysis (EDX) was measured on an Aztec X-Max Extreme EDS. Reflection spectra were recorded on an Ideaoptics Instruments angle-resolved spectrum system (400–800 nm). Ultraviolet-visible diffuse reflectance was performed on Shimadzu UV-3600. XPS was conducted on a Thermo Scientific K-Alpham from Shiyanjia Lab (www.shiyanjia.com). The Fourier-transform infrared spectra of the sample were recorded on Thermofisher Nicolet 6700. The atomic force microscopy (AFM) was performed on Fastcan A61-1. Electrochemical synthesis experiments were carried out on the CHI660 (Shanghai, China).

Preparation of PS arrays.

Fluorine-doped tin oxide conductive glass (FTO, about 2 $\times$ 1 cm^2) was washed in ethanol and deionized water for 20 minutes and stored in ethanol before use. 0.1 mL PS solution (10 wt%) was added into 4.9 mL aqueous solution with a surfactant and then the mixture was ultrasonicated for several minutes. The surfactant reduced interfacial tension, which repressed the formation of cracks in the PS arrays. The FTO was treated with oxygen plasm for 2 min and then put into the solution. The whole

device was placed at 65 °C oven for several days.

Fabrication of the hierarchical ordered macropores BHP-MOFs

35.68 mg (0.08 mmol) of $Eu(NO_3)_3 \cdot 6H_2O$, 326.18 mg (0.72 mmol) of $Tb(NO_3)_3 \cdot 5H_2O$, 68.8 mg (0.4 mmol) of thiphene-2,5-dicarboxylic acid (TDA) and 0.7 mg sodium acetate were dissolved in 40 mL solution. A classic two-electrode cell was used in this electrodeposition process. FTO coated with PS arrays was used as a working electrode, with graphite as the counter electrode. The two electrodes were applied with a constant current of –0.4 mA/cm^2 for a certain time until the PS arrays filled with MOFs particles. Then the substrate was immersed in the THF solutions to remove the template PS spheres. In this time, three-dimensional ordered hierarchical porous MOF film was constructed.

Optical Response Measurement:

The fluorescent BHP-MOF films prepared on the FTO slides were placed diagonally in the quartz cuvette and sealed, which was then placed in the Edinburgh FLS 1000 for luminescent measurements. The excitation wavelengths were scanned over 200–450 nm at an increment of 1 nm while activating emissions at 612 nm or 544 nm. To obtain the emission spectra at the 310 nm, the emission scans started from 400 nm until 750 nm at an increment of 1 nm. Average value was obtained by the repeating measurement twice.

DFT calculations:

DFT calculations were performed by Gaussian 16 software (Revision A.03). Geometry optimizations and frequency analyses for all molecules were calculated by Becke3LYP (B3LYP) hybrid functional with triple zeta valence basis set def$_2$-TZVP. All the optimized molecular geometry was confirmed to energy minima according to the results of the frequency analysis, and then the energies of HOMO and LUMO for the molecules were acquired. The molecular orbitals were visualized by the GaussView6 software (Revision 6.0.16).

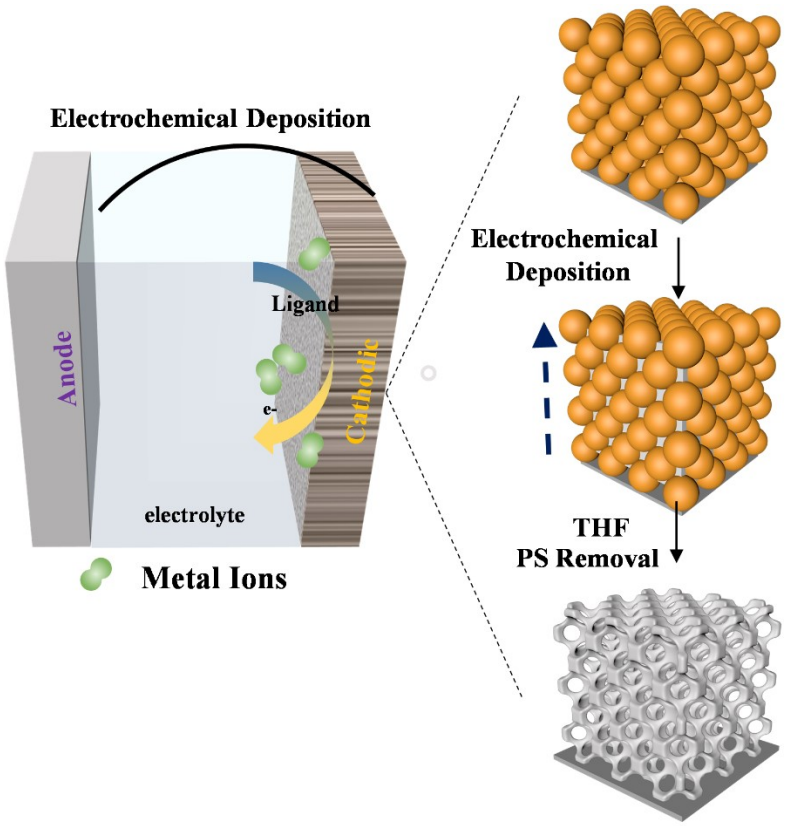

Fig. S1. Schematic illustration of the preparation of bimetallic MOFs with three-dimensionally ordered microporous structure, which can generate structural and fluorescent color and serve as dynamic photonic materials towards different analytes.

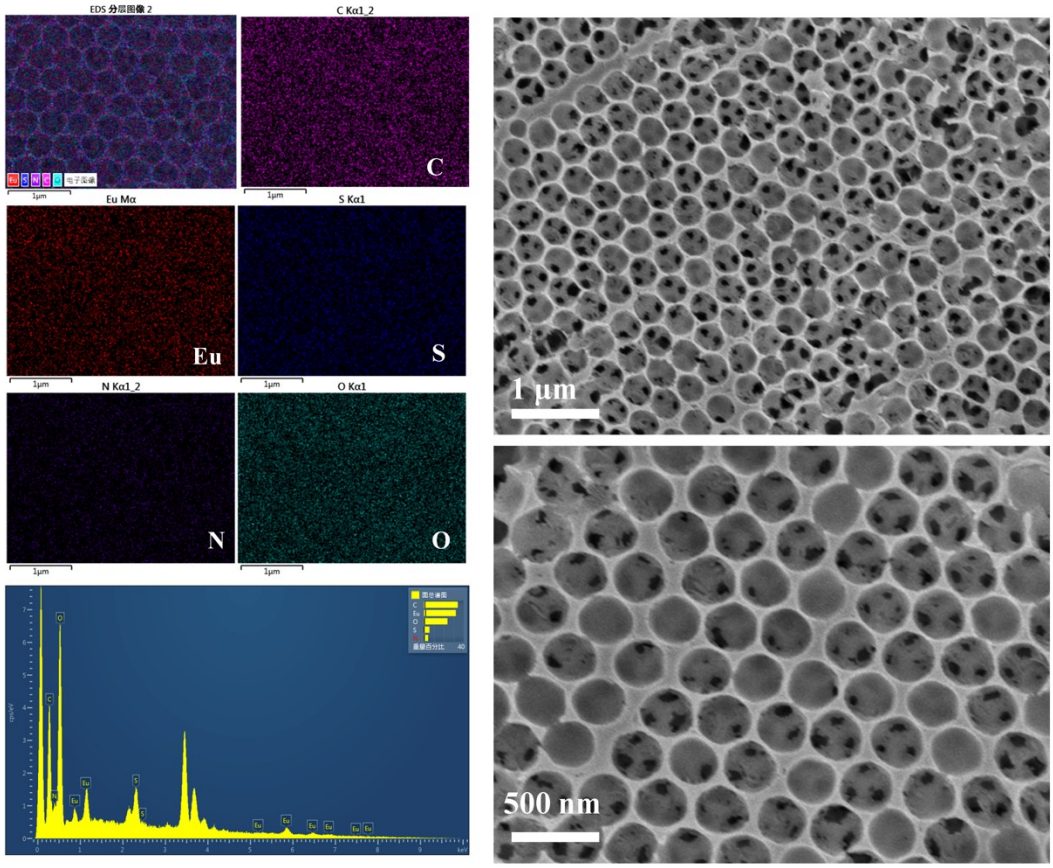

Fig. S2. SEM images and the corresponding elemental mappings of HP-Eu-MOFs.

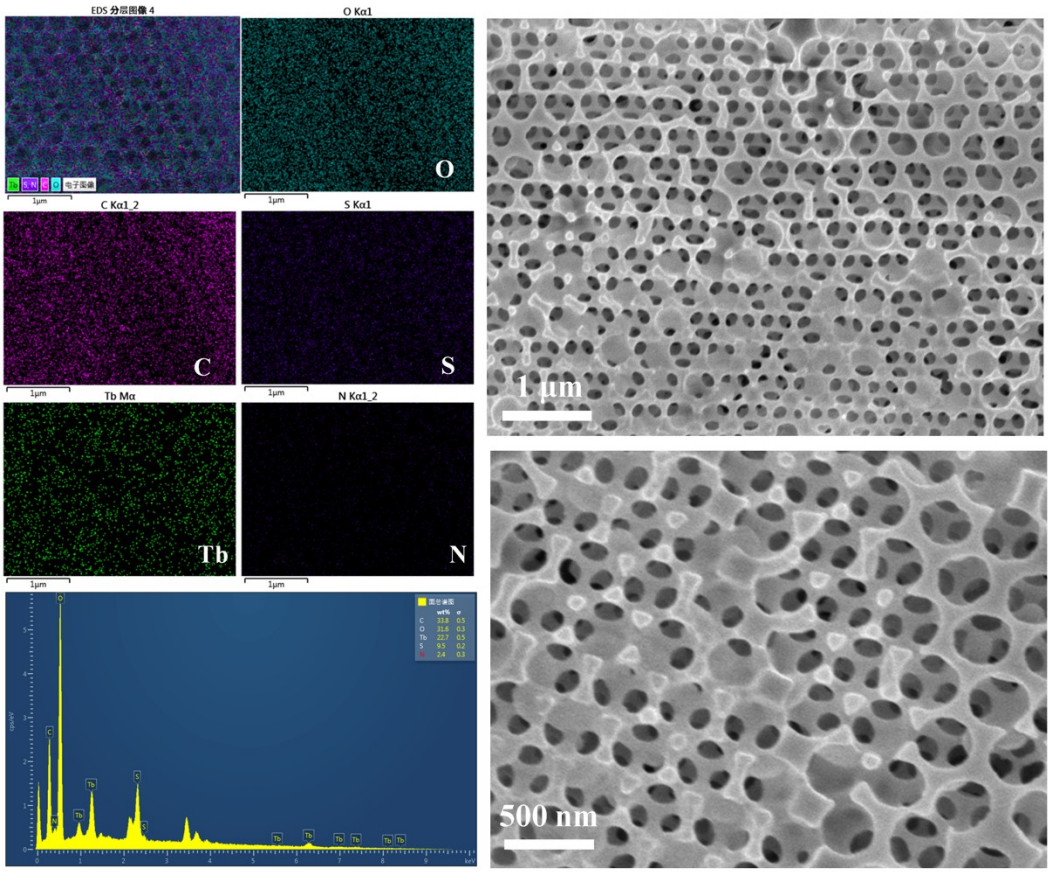

Fig. S3. SEM images and the corresponding elemental mappings of the HP-Tb-MOFs.

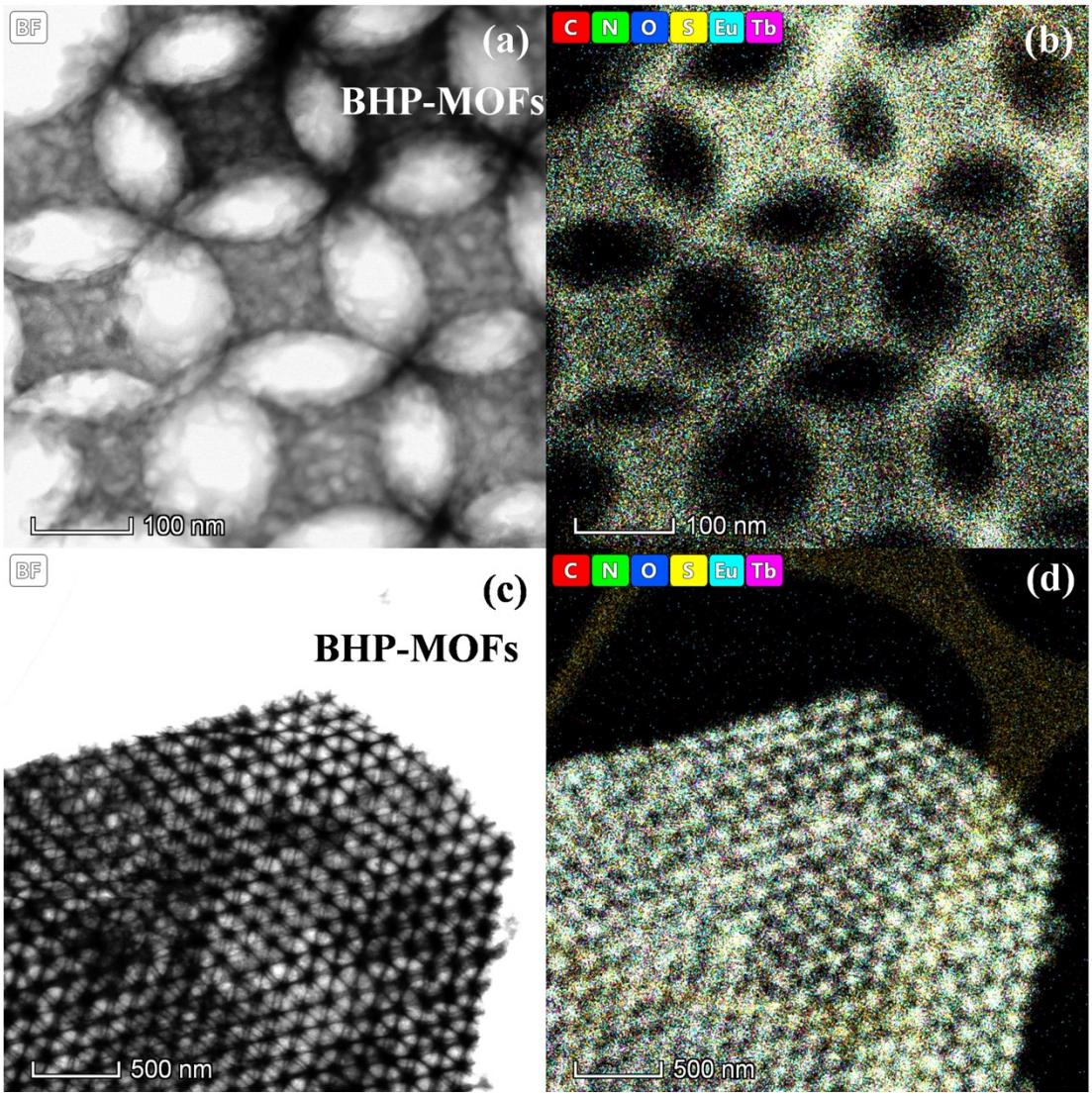

Fig. S4. (a) High-resolution TEM image and (c) low-magnification TEM image, (b) and (d) corresponding EDS mapping of the hierarchical BHP-MOFs, where ordered macropores could be observed clearly.

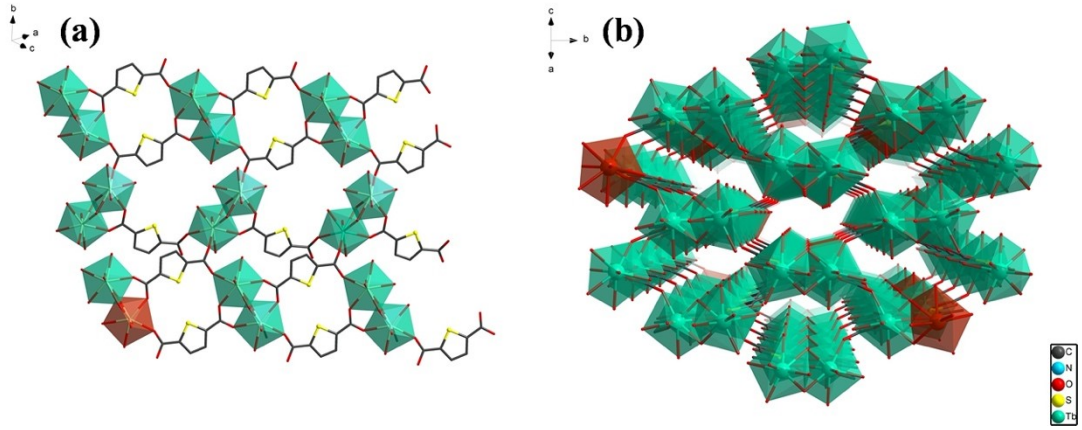

Fig. S5. 3D framework of the bimetallic MOFs. (Tb: green polyhedral, Eu: red polyhedral, C: black, O: red, S: yellow).

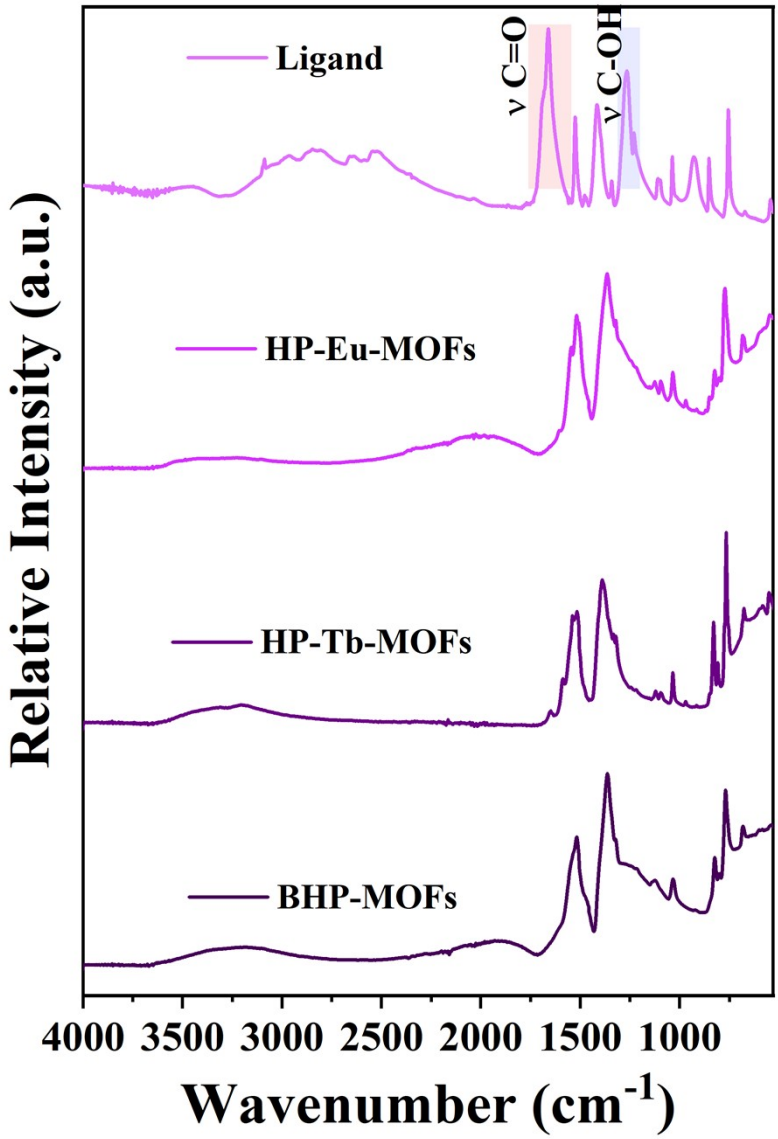

Fig. S6. FTIR spectra of the ligand H_2TDA reactant, HP-Eu-MOFs, HP-Tb-MOFs, and BHP-MOFs. The ligand TDC exhibits the C=O stretching vibration band at 1664 cm^{-1} and O-H wagging vibration band at 1271–1290 cm^{-1} of nonionized carboxy groups. These vibration bands disappear in synthesized MOF films, which can be assigned to the lanthanide ions bonded to the oxygen of ligands.

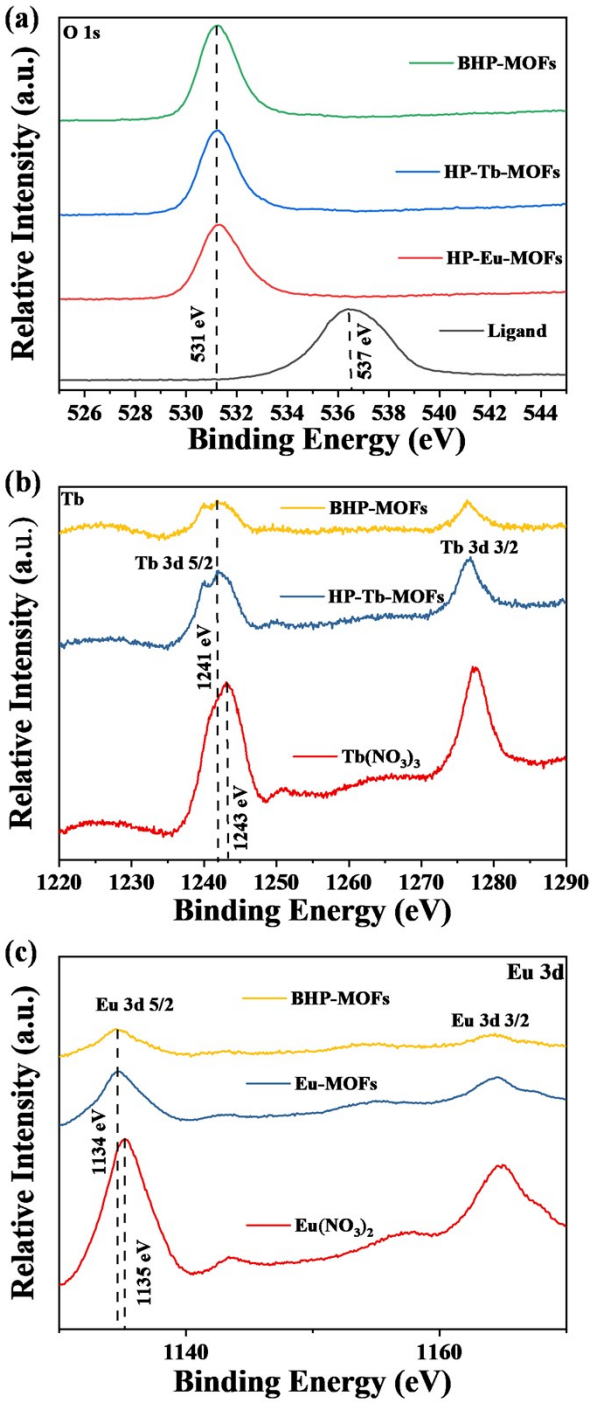

Fig. S7. XPS spectra of (a) O 1s, (b) Tb 3d, and (c) Eu 3d in BHP-MOFs.

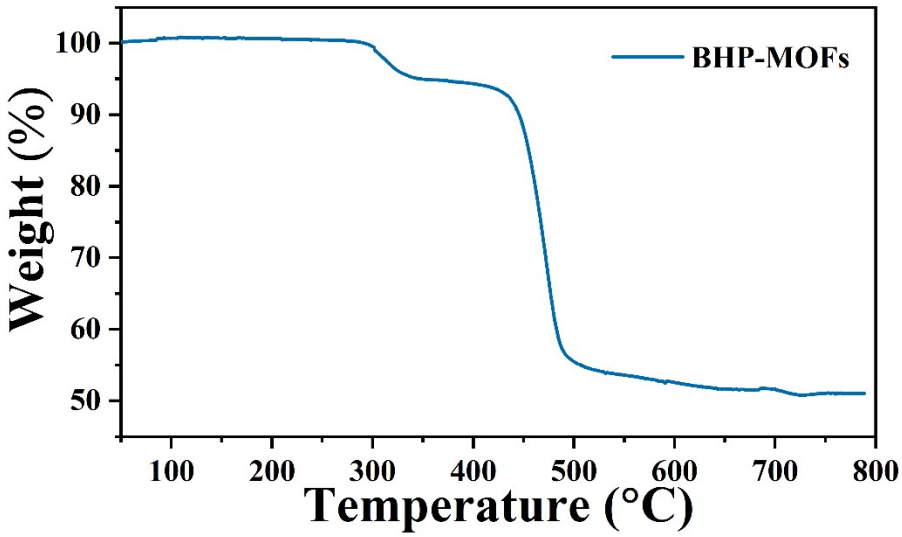

Fig. S8. TGA curves for BHP-MOFs under N_2 atmosphere at the range of 50–800 °C.

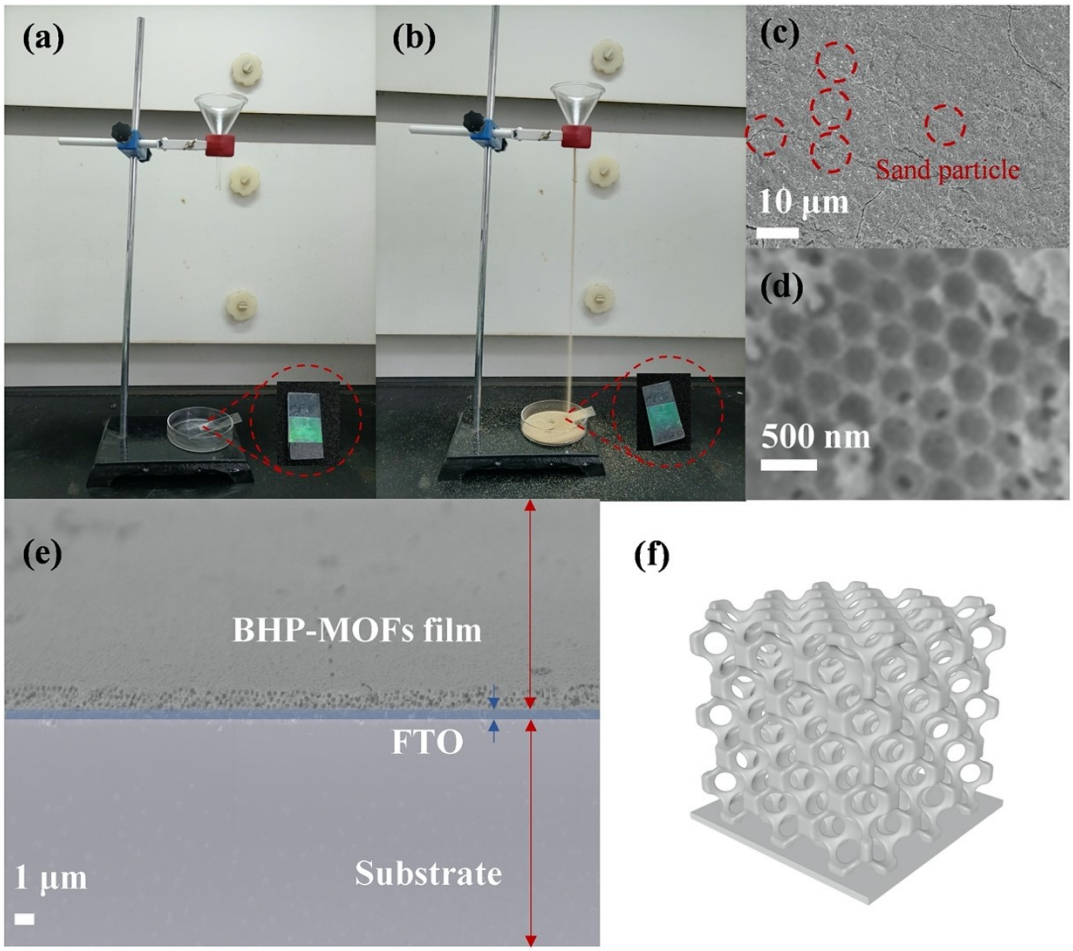

Fig. S9. (a–b) Stability of BHP-MOFs by sand abrasive test driven by gravity. Inset is the photograph of this film before and after treated with sand. (c–d) The SEM image of BHP-MOFs at low and high magnification. (e) Cross-sectional image and (f) illustration of BHP-MOFs on the FTO substrate.

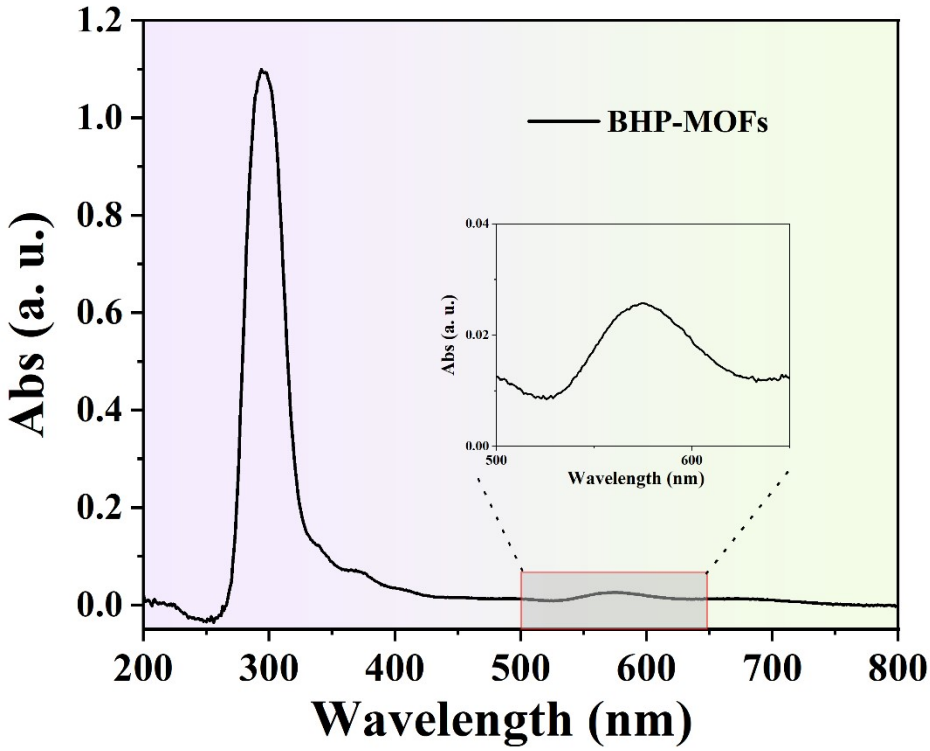

Fig. S10. UV-vis spectrum of the BHP-MOFs. Intrinsic structure and ordered macropores resulted in two absorption peaks in the spectrum.

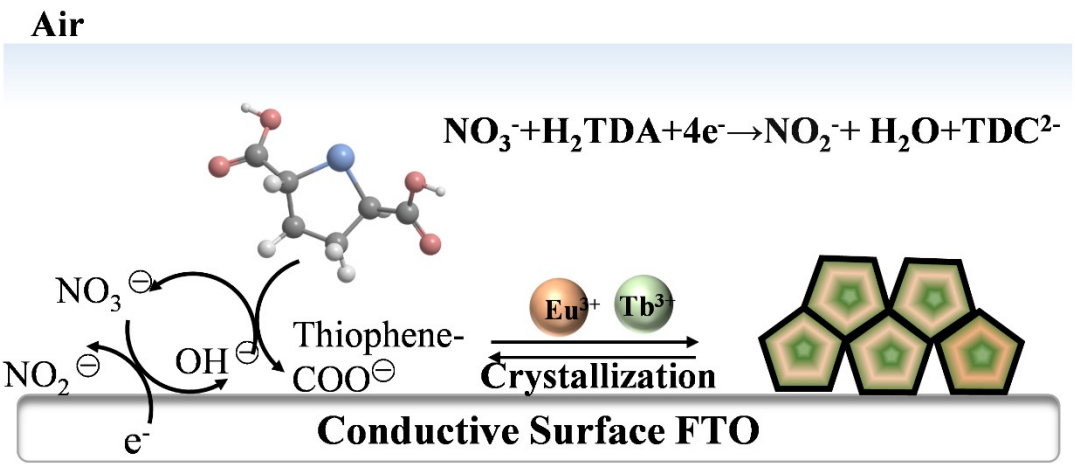

Fig. S11. General scheme for the cathodically-induced electrochemical deposition of MOFs, involving the deprotonation of ligands, and the MOFs crystallization.

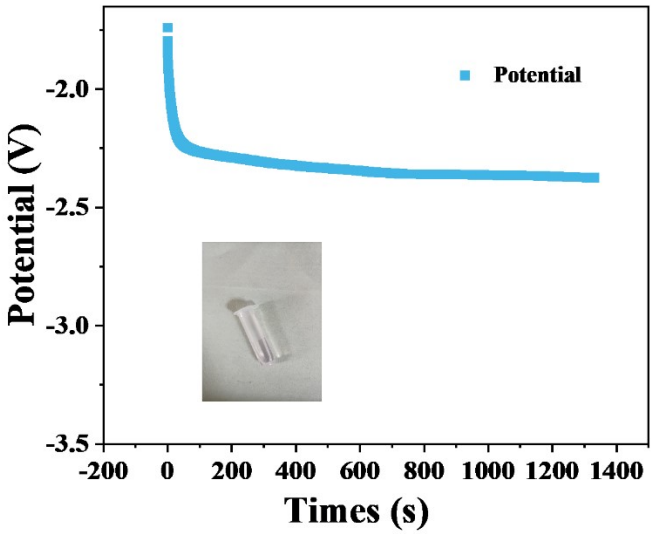

Fig. S12. The change of voltage during the film synthesis, as detected by the CHI electrochemical working station. Inset image: detection of the existence of NO_2^- in the remanent solution using the Griess reagent. The indicator reagent turns light pink, indicating the generation of NO_2^- in the spent solution.

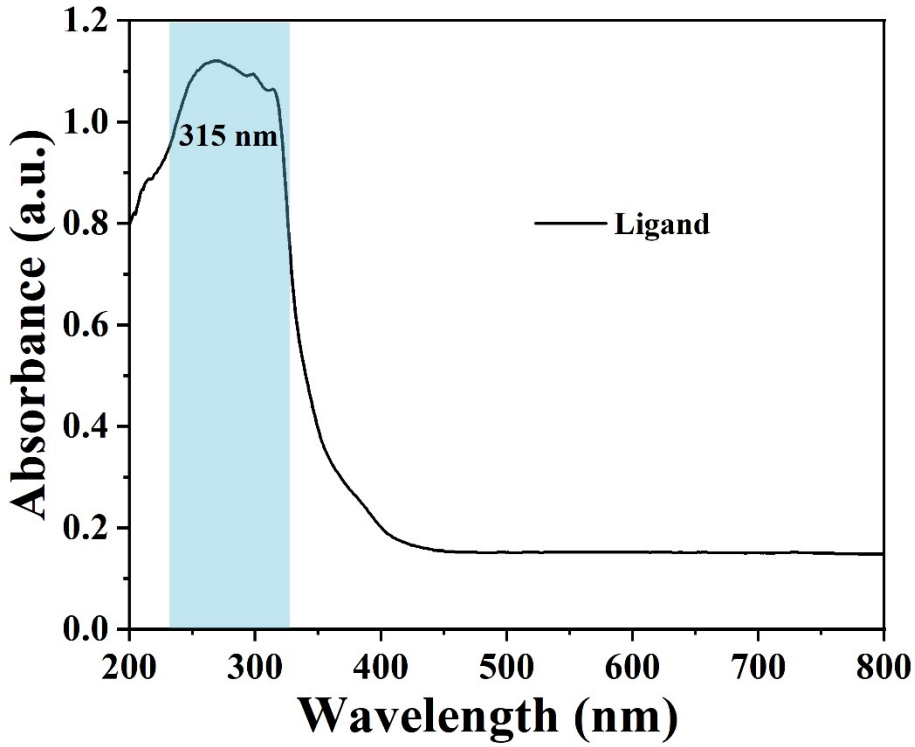

Fig. S13. UV-vis diffuse reflection spectrum of the solid ligand. An absorption peak was located at 315 nm with the single state (S_1) at approximately 31,764 cm^{-1}.

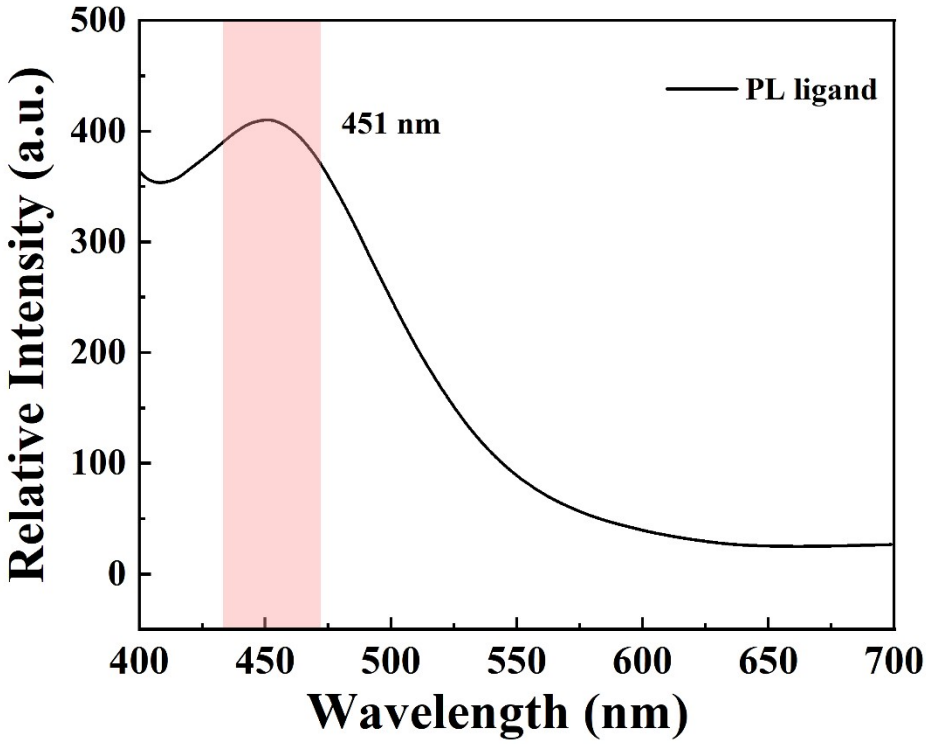

Fig. S14. Phosphorescence emission spectrum of the ligand in solid-state monitored at 77 K. A phosphorescence peak is observed at approximately 451 nm.

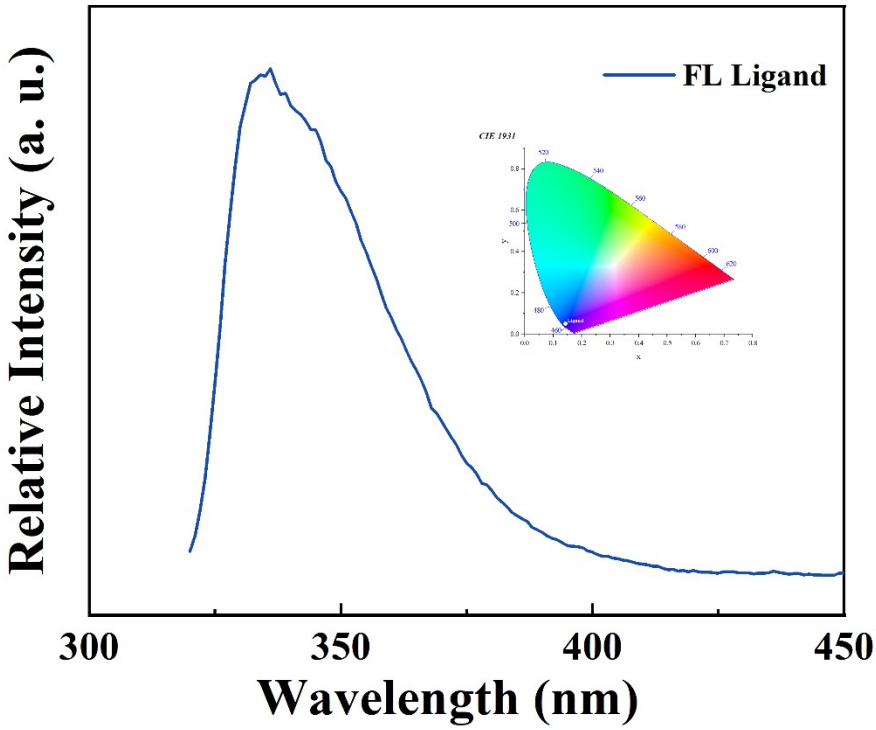

Fig. S15. Fluorescence emission spectrum of ligand. Inset shows the corresponding CIE image.

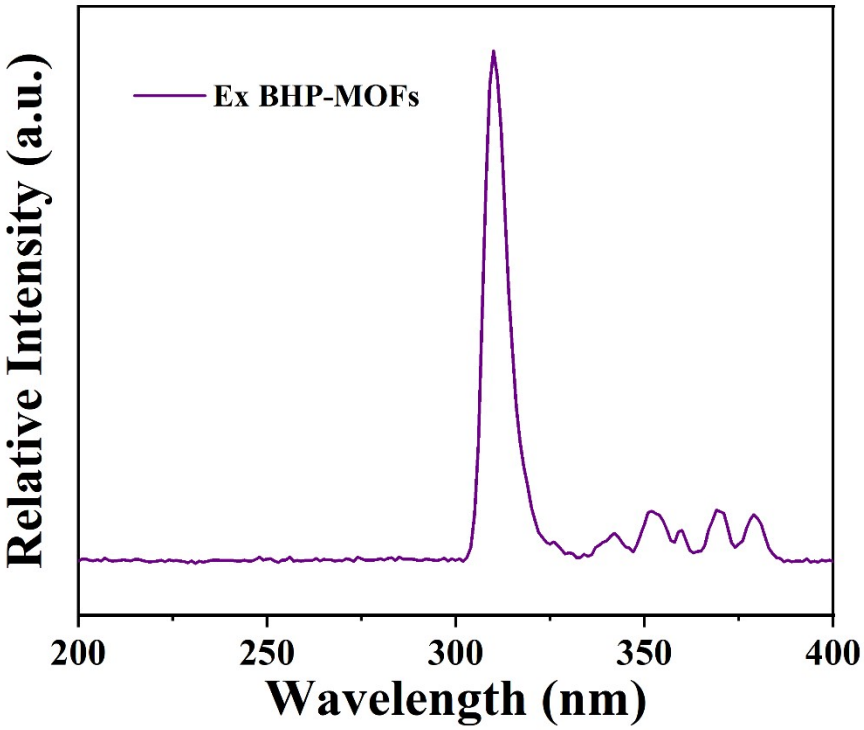

Fig. S16. Fluorescence excitation spectrum of the BHP-MOFs solid.

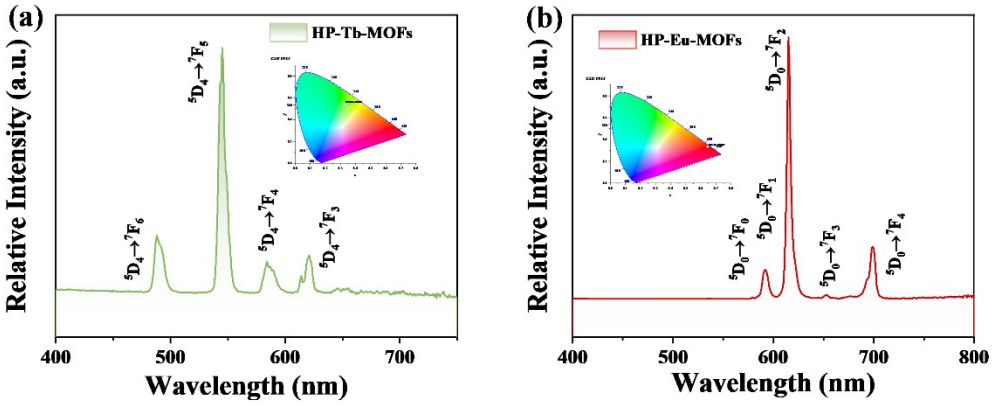

Fig. S17. Fluorescence emission spectrum of (a) HP-Tb-MOFs and (b) HP-Eu-MOFs. Inset shows the corresponding CIE image.

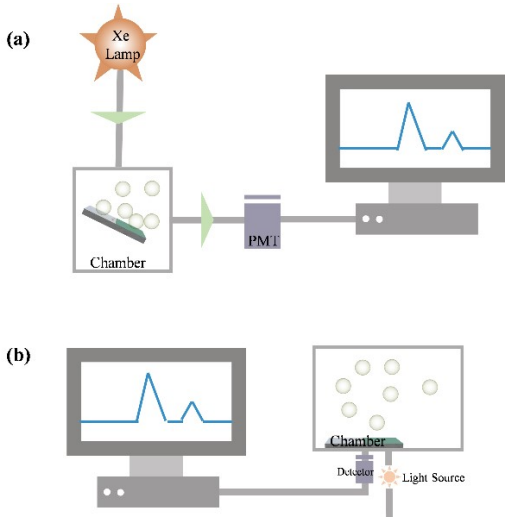

Fig. S18. Schematic drawing of the VOAs vapor testing measurement setup used in (a) fluorescence and (b) reflection mode.

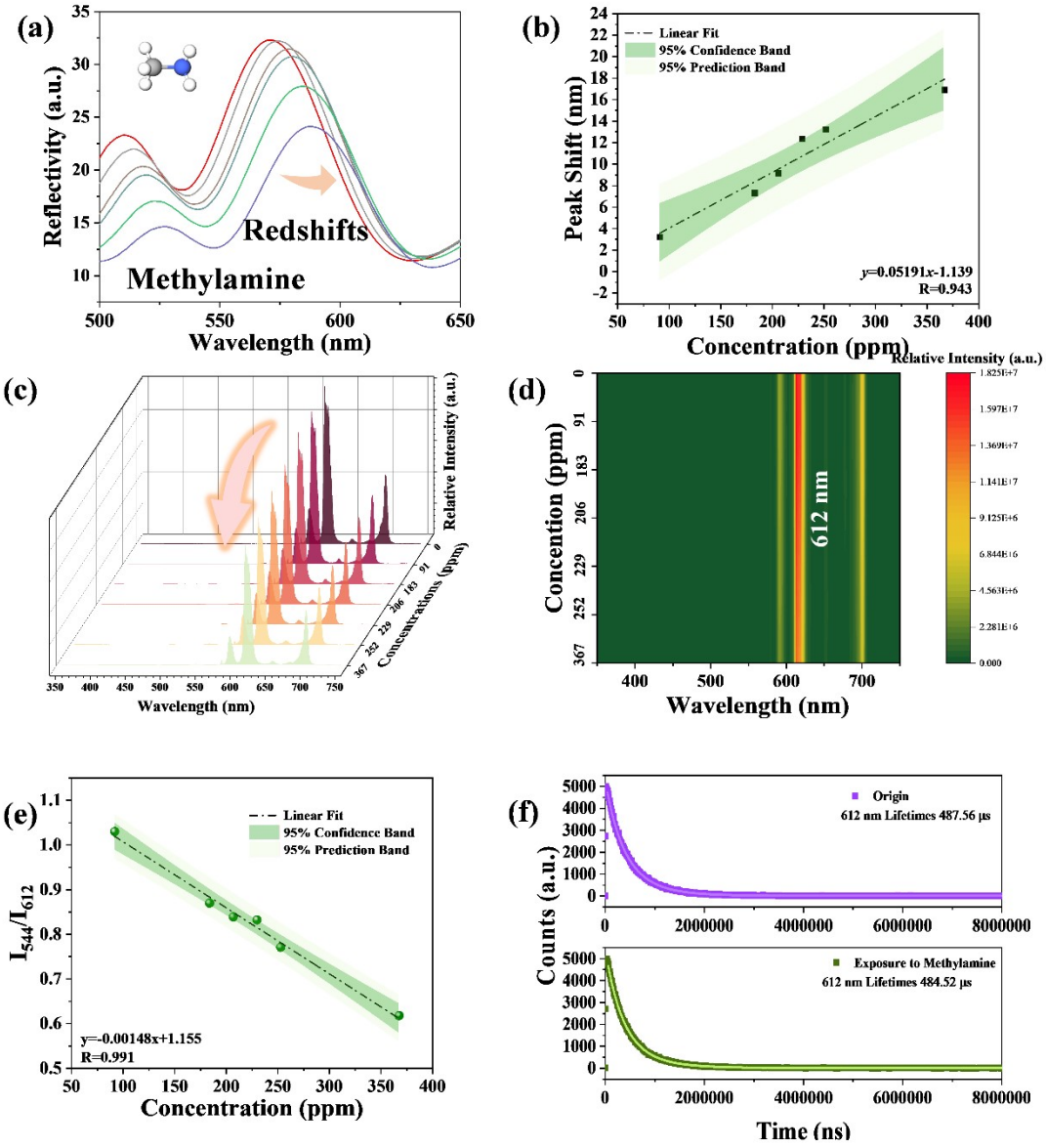

Fig. S19. (a) Reflectance spectra of the peak shift after treatment with different concentrations of methylamine, and (b) linear relationship between the corresponding peak shift and concentrations. (c) Emission spectra and (d) contour map of BHP-MOFs exposed to methylamine at different concentrations, (e) plot of I_{544}/I_{612} versus concentrations; (f) luminescence lifetimes of 612 nm before and after treatment with methylamine.

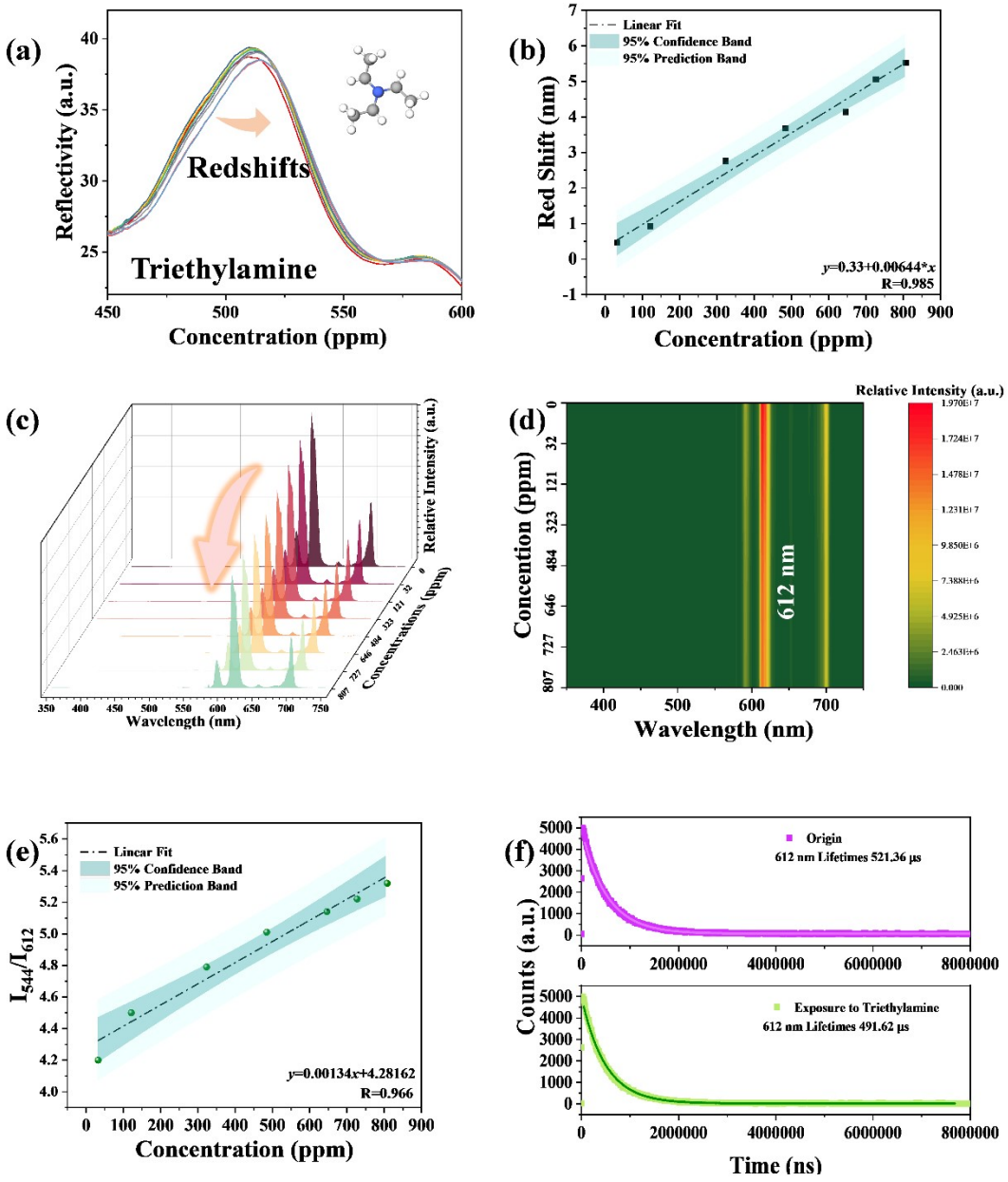

Fig. S20. (a) Reflectance spectra of the BHP-MOFs exposed at the triethylamine, and (b) the corresponding linear fit. The concentration-dependent (c) photoluminescence spectra and (d) contour map of BHP-MOFs towards triethylamine, the corresponding (e) linear fit; (f) luminescence lifetimes before and after treatment with triethylamine.

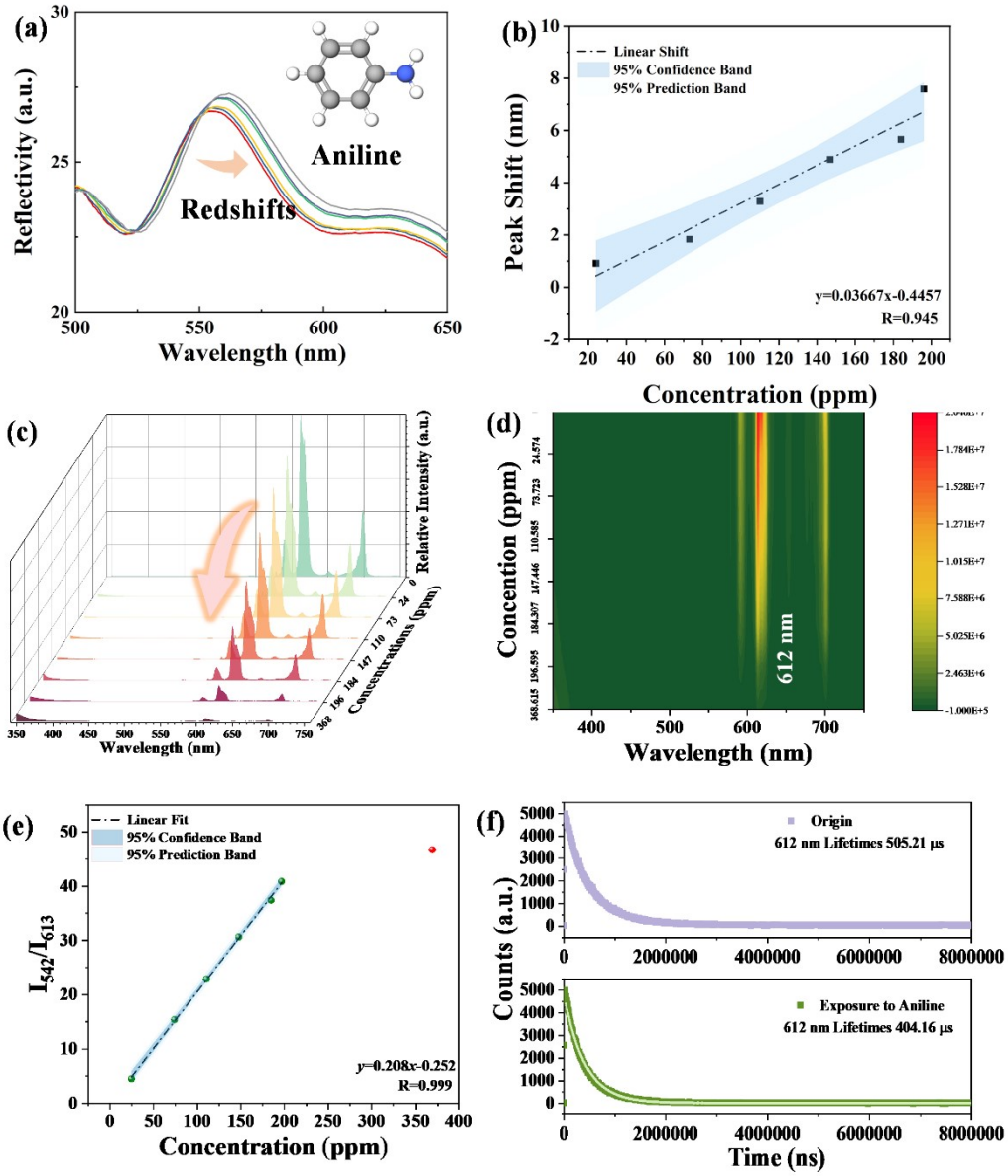

Fig. S21. (a) Reflectance spectra of the peak shift after treatment with different concentrations of aniline, and (b) linear relationship between the corresponding peak shift and concentrations. (c) Emission spectra and (d) contour map of BHP-MOFs exposed to aniline at different concentrations, (e) plot of I_{544}/I_{613} versus concentrations; (f) luminescence lifetimes of 612 nm before and after treatment with aniline.

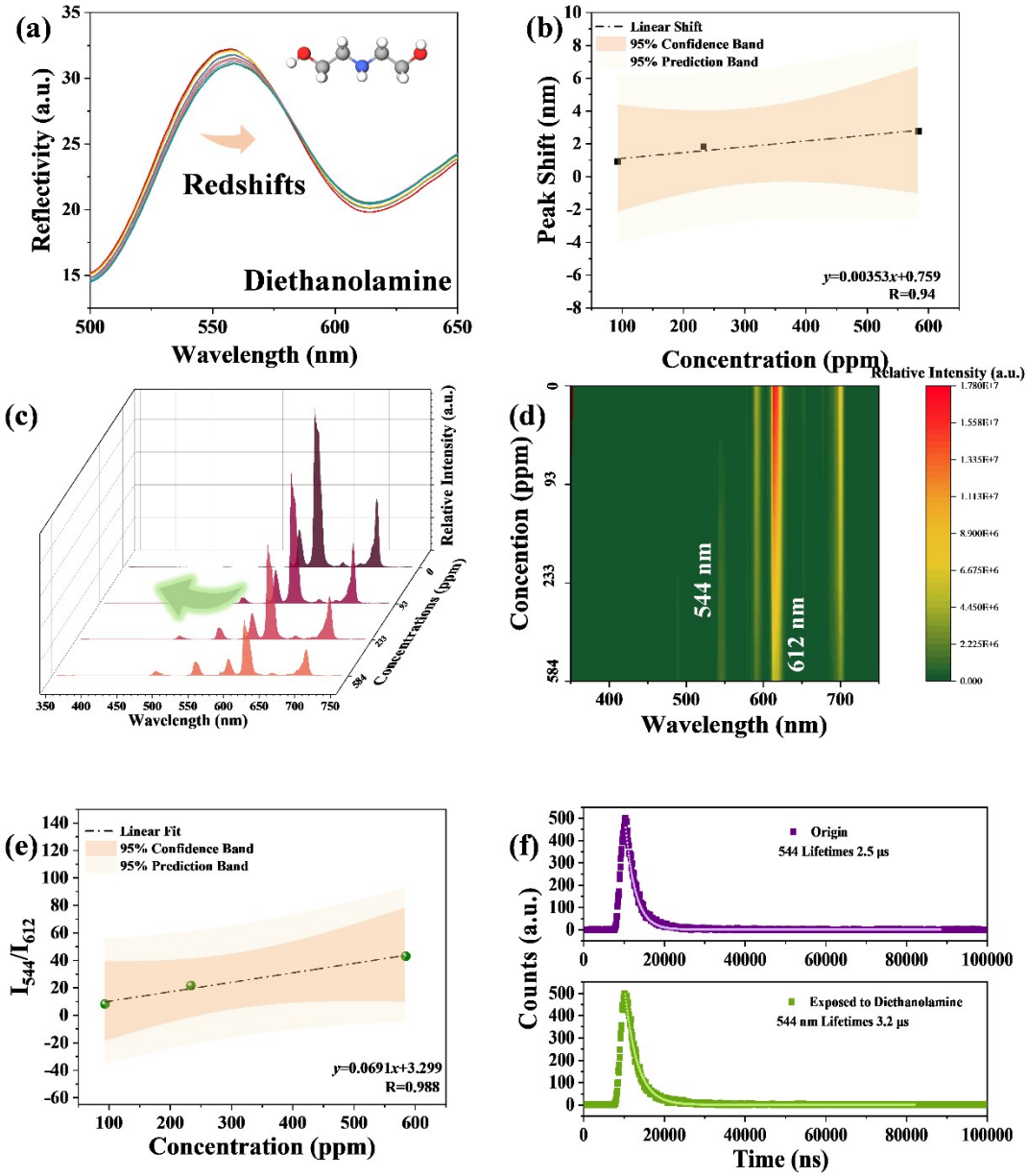

Fig. S22. (a) The reflectance spectra of the BHP-MOFs in different concentration, and the (b) fitted line plot. (c) Luminescence emission and (d) contour map turn-on spectra upon the incremental concentrations of diethanolamine, (e) and the corresponding linear fit; (f) lifetimes of 544 nm before and after exposure to diethanolamine.

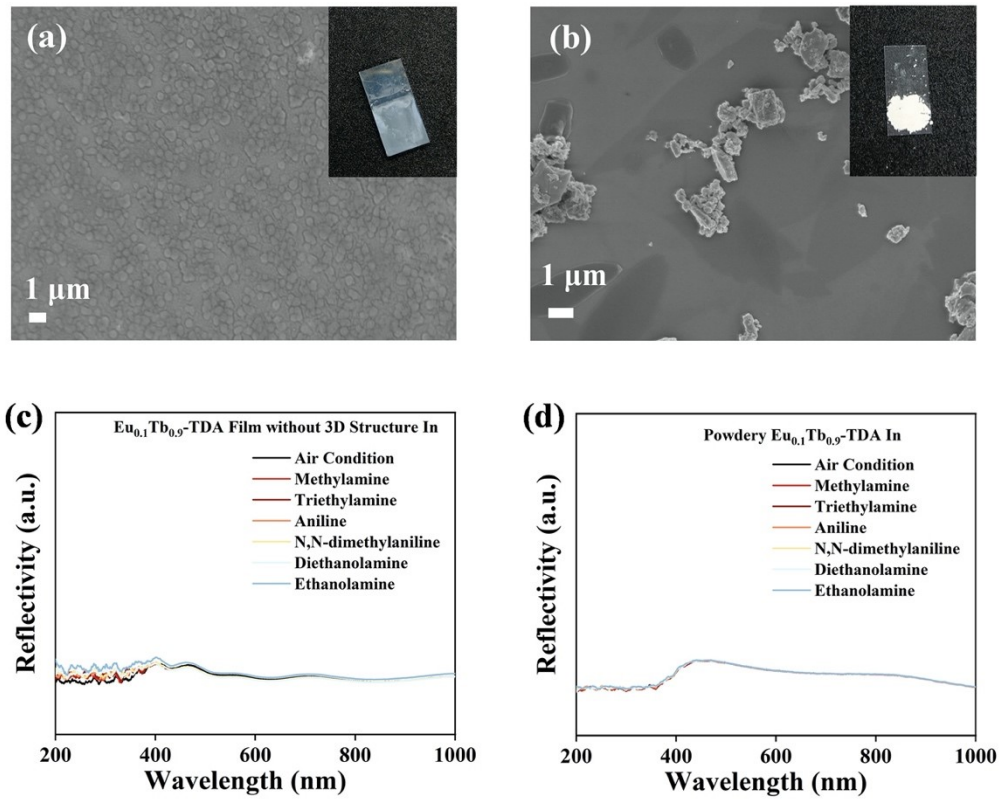

Fig. S23. The SEM image of (a) $Eu_{0.1}Tb_{0.9}$-TDA film without macropores and (b) powdery $Eu_{0.1}Tb_{0.9}$-TDA, inset in (a–b) shows the photograph of the film and powdery. Reflectance spectra of (c) $Eu_{0.1}Tb_{0.9}$-TDA film and (d) powdery $Eu_{0.1}Tb_{0.9}$-TDA in air condition and six kinds of VOAs.

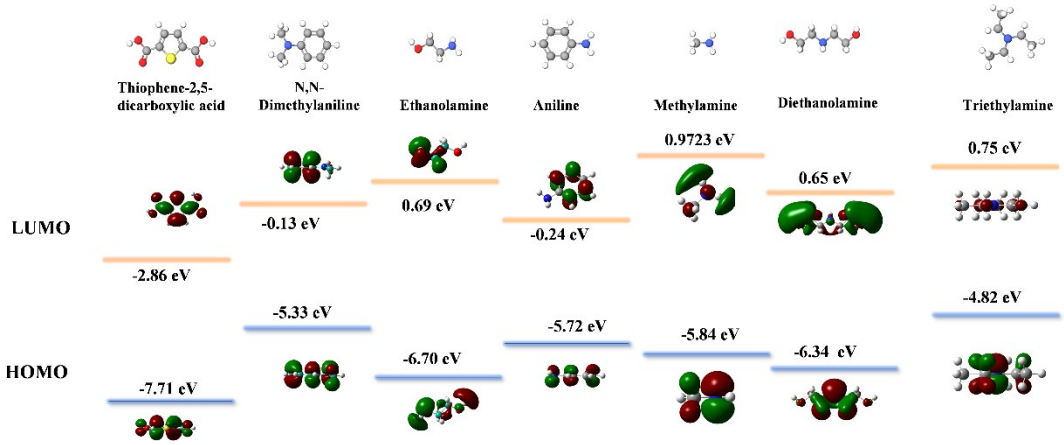

Fig. S24. LUMO–HOMO of ligand and organic amines.

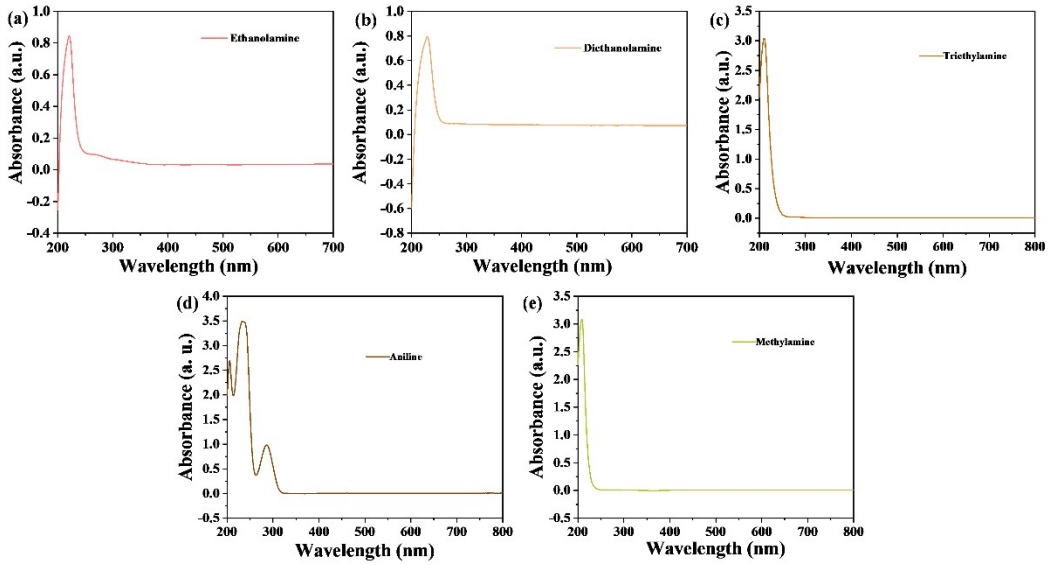

Fig. S25. The UV-vis spectra of (a) ethanolamine, (b) diethanolamine, (c) triethylamine, (d) aniline, and (e) methylamine.

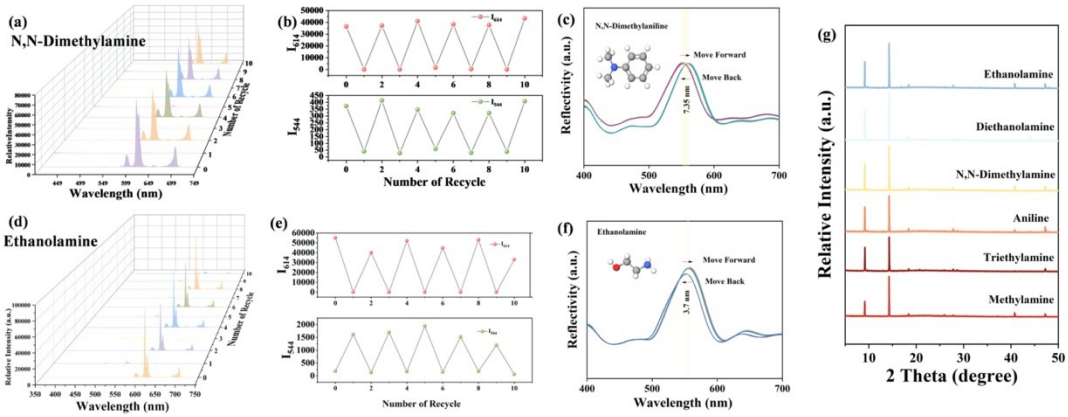

Fig. S26. Recovery tests of BHP-MOFs in (a–b) N,N-dimethylamine and (d–e) ethanolamine atmosphere in fluorescence mode, and (c) N,N-dimethylamine (f) N,N-dimethylamine in reflectance mode. It suggested that the BHP-MOFs is recyclable for decoding VOAs. (g) The XRD patterns of NHP-MOFs samples treating with VOAs, which verified the BHP-MOFs retained a rigid and stable framework after adsorbing different VOAs.

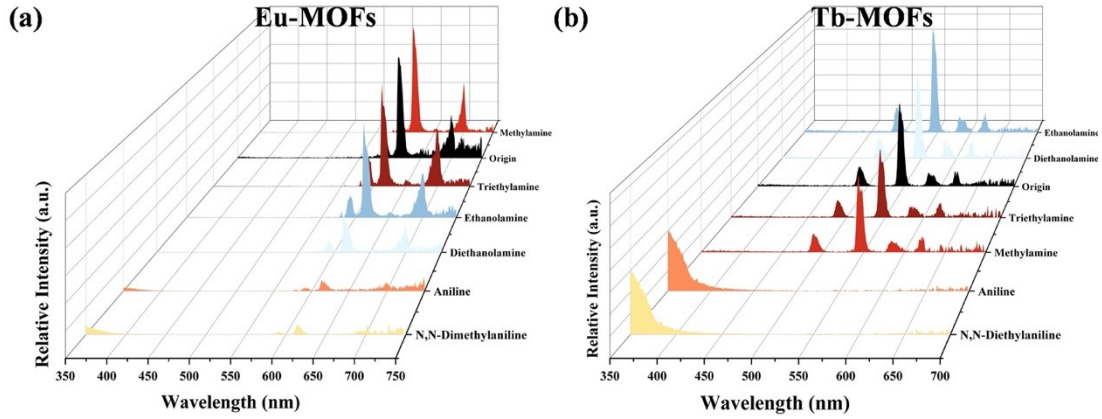

Fig. S27. The emission spectra of (a) Eu-MOFs (b) Tb-MOFs recorded in six different kinds of VOAs atmosphere. As compared with single lanthanide ions emission intensity-based method, bimetallic BHP-MOFs are expected to be more reliable and accurate.

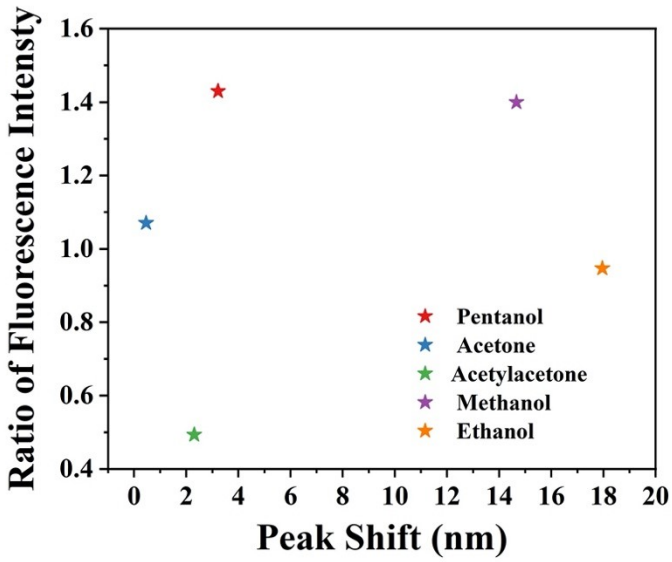

Fig. S28. A two-dimensional decoded map of five materials (pentanol, acetone, acetylacetone, methanol, and ethanol) in saturated concentration based on the peak shifts and the emission intensity ratio (I_{544}/I_{612}).

Table S1. The lifetimes and quantum yields of $^5D_4$ of Tb^{3+} and $^5D_0$ of Eu^{3+} for Eu-MOFs, Tb-MOFs and BHP-MOFs. The decay curves are monitored at 544 nm and 615 nm and excited at 310 nm. The quantum yields of Eu^{3+} increased and the Tb^{3+} decreased owing to the additional energy transfer pathway from Tb^{3+} to Eu^{3+}.

Materials	**$^5D_4$ of Tb^{3+} (μs)**	**$^5D_0$ of Eu^{3+} (μs)**	**Quantum Yield**	
Eu-MOFs	/	329	4.42%	
Tb-MOFs	37	/	36.48%	
BHP-MOFs	5	473	1.03%	6.03%

Table S2. The concentration of vapor was calculated from equation. In this formula, c (ppm) refers to the concentration of the volatile organic amine, ρ (g/mL) is the density of the alcohols, *V* (mL) represents the volume of the alcohols, *M* (g/mol) is the molecular weight, and V_0 (mL) denotes the volume of the gas chamber (20 × 10 × 20 mL).

$$c = \frac{(\rho V/M)}{V_0/(22.4L/mol)} = \frac{22.4\rho V}{MV_0} \times 10^6$$